Tuning of spin-orbit coupling in chiral molecule-incorporated two-dimensional organic-inorganic hybrid perovskite copper halides with ferromagnetic exchange interactions

Kouji Taniguchi [1,2,*] Po-Jung Huang,[1] Hajime Sagayama,[3] Ryoji Kiyanagi [4] Kazuki Ohishi [5] Shunsuke Kitou,[6,†]
Yuiga Nakamura,[7] and Hitoshi Miyasaka[8,9]

[1]*Department of Chemistry, School of Science, Tokyo Institute of Technology, 2-12-1 Ookayama, Meguro-ku, Tokyo 152-8551, Japan*
[2]*PRESTO, Japan Science and Technology Agency (JST), 5-3 Yonbancho, Chiyoda-ku, Tokyo 102-8666, Japan*
[3]*Institute of Materials Structure Science, High Energy Accelerator Research Organization, Tsukuba 305-0801, Japan*
[4]*J-PARC Center, Japan Atomic Energy Agency, Tokai, Ibaraki 319-1195, Japan*
[5]*Neutron Science and Technology Center, Comprehensive Research Organization for Science and Society (CROSS),
Tokai, Ibaraki 319-1106, Japan*
[6]*RIKEN Center for Emergent Matter Science, Wako 351–0198, Japan*
[7]*Japan Synchrotron Radiation Research Institute (JASRI), SPring-8, Hyogo 679-5198, Japan*
[8]*Institute for Materials Research, Tohoku University, 2-1-1 Katahira, Aoba-ku, Sendai 980-8577, Japan*
[9]*Department of Chemistry, Graduate School of Science, Tohoku University, 6-3 Aramaki-Aza-Aoba,
Aoba-ku, Sendai 980-8578, Japan*

Leveraging the flexible material designability of organic-inorganic hybrid systems, spatial inversion symmetry breaking and spin-orbit coupling (SOC) were simultaneously controlled in a series of two-dimensional organic-inorganic hybrid perovskite (2D-OIHP) copper halides with ferromagnetic exchange interaction (FMI). In chiral molecule-incorporated 2D-OIHP copper halides, an increase in Br component over Cl component at halogen sites leads to systematic variations in magnetic phase diagrams owing to the competition between the FMI and Dzyaloshinskii-Moriya interaction induced by the SOC. The crucial role of noncentrosymmetry in the competition for the magnetic interactions was confirmed by comparing the magnetic phase diagrams of chiral and achiral 2D-OIHP copper bromides.

I. INTRODUCTION

Spin-orbit coupling (SOC) in noncentrosymmetric systems has opened up various avenues for research on novel spin-related phenomena. For example, SOC has been found to induce spin-momentum locking states by the Rashba effect in noncentrosymmetric semiconductors [1,2], nonreciprocal directional charge transport in chiral/polar conductors [3–7], and gigantic magnetoelectric effect in multiferroics with spiral spin structures [8–12]. In addition, noncentrosymmetric ferromagnetic spin systems are promising candidates for realizing noncollinear/noncoplanar spin states characterized by long-period magnetic modulation vectors, such as helical spin structures [13,14] and magnetic skyrmions [15–18], through the competition between ferromagnetic exchange interaction (FMI) and the Dzyaloshinskii-Moriya interaction (DMI) originating from SOCs. They have recently attracted attention as a platform for investigating emerging electromagnetic responses, such as the topological Hall effect [19,20] and magnetochiral electrical transport [21,22].

Two-dimensional organic-inorganic hybrid perovskite (2D-OIHP) emerges as a promising platform for designing noncentrosymmetric ferromagnetic spin systems. In 2D-OIHPs, the spatial inversion symmetry can be intentionally broken by incorporating chiral molecules into the van der Waals gap between the inorganic layers [Figs. 1(a) and 1(b)]. To date, chiral molecule-incorporated 2D-OIHPs have been reported to exhibit various types of noncentrosymmetry-induced physical phenomena, such as circular dichroism [23–25], circularly polarized luminescence [24–27], ferroelectricity [28], bulk photovoltaic effect [29,30], circular photogalvanic effect [31,32], chirality-induced spin selectivity [33–35], and nonreciprocal directional dichroism [36,37]. In the design of magnetic systems, spins can be introduced into 2D-OIHPs using transition metal ions, such as Cu^{2+}, Cr^{2+}, Mn^{2+}, and Fe^{2+}, as components of the inorganic layers in the 2D-OIHPs [36–40]. In particular, 2D-OIHP copper halides exhibit ferromagnetism owing to their orbital ordering, which is characterized by an orthogonal $3d$-orbital arrangement [Figs. 1(c) and 1(d)] [41,42]. Therefore, chiral molecule-incorporated 2D-OIHP copper halides are suitable for exploring the nontrivial long-periodic magnetic phases produced by the competition between the FMI and DMI.

In this study, we demonstrate that the strength of SOC can be tuned in chiral-molecule-incorporated 2D-OIHP copper halides by replacing halogen atoms with larger atomic

*taniguchi.k.ap@m.titech.ac.jp
†Present address: Department of Advanced Materials Science, The University of Tokyo, Kashiwa 277-8561, Japan.
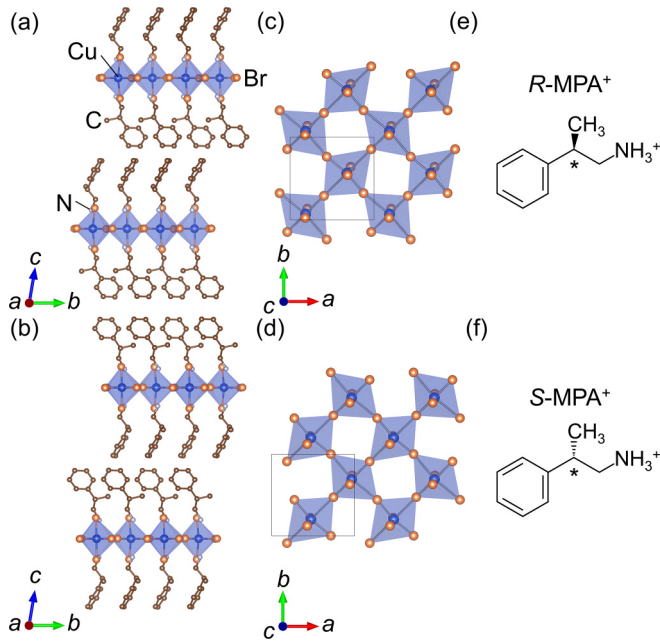
FIG. 1. Crystal structures projected along the a axis of (a) $(R\text{-MPA})_2\text{CuBr}_4$ and (b) $(S\text{-MPA})_2\text{CuBr}_4$. $[\text{CuBr}_4]^{2-}$ layer structures along the c axis of (c) $(R\text{-MPA})_2\text{CuBr}_4$ and (d) $(S\text{-MPA})_2\text{CuBr}_4$. The crystal structures of $(R\text{-MPA})_2\text{CuBr}_4$ and $(S\text{-MPA})_2\text{CuBr}_4$ were measured at 30 K. Blue, orange, brown, and gray atoms represent Cu, Br, C, and N, respectively. Hydrogen atoms are omitted for clarity. Molecular cation structures of (e) $R\text{-MPA}^+$ and (f) $S\text{-MPA}^+$.

number. As the competition between FMI and DMI is intensified, systematic magnetic phase changes have been observed from the ferromagnetic phase of 2D-OIHP copper chlorides to multiple magnetic-order phases of 2D-OIHP copper bromides. In addition, the magnetic phase diagrams of the noncentrosymmetric and centrosymmetric 2D-OIHP copper bromides have been compared to confirm the origin of the magnetic phase variation.

II. EXPERIMENTAL

A. Synthesis of chiral molecule-incorporated 2D-OIHP copper halides

The developed chiral-molecule-incorporated 2D-OIHP copper halides are $(R\text{-MPA})_2\text{Cu}(\text{Cl}_{1-x}\text{Br}_x)_4$ ($x = 0$, 0.25, 0.5, 0.75, 1), $(S\text{-MPA})_2\text{CuBr}_4$, and deuterated $(R\text{-MPA})_2\text{CuBr}_4$ ($D\text{-}R\text{-MPA-Br}$), where $R/S\text{-MPA}^+$ represents $(R/S)\text{-}\beta$-methylphenethylammonium ion [Figs. 1(e) and 1(f)]. Platelike yellow single crystals of $(R\text{-MPA})_2\text{CuCl}_4$ ($x = 0$) were grown according to a procedure reported in our previous study [37]. Platelike dark-violet single crystals of $(R/S\text{-MPA})_2\text{CuBr}_4$ ($x = 1$) were grown by evaporating a mixture of an aqueous HBr solution of CuBr and a methanol solution of $(R/S)\text{-}\beta$-methylphenethylamine. Single crystals of the solid-solution compounds of chloride and bromide, such as $(R\text{-MPA})_2\text{Cu}(\text{Cl}_{1-x}\text{Br}_x)_4$ ($x = 0.25$, 0.5, and 0.75), were grown by a procedure similar to that for $x = 1$, using a mixed solution of HCl and HBr. The single crystals of $D\text{-}R\text{-MPA-Br}$ were synthesized similarly to $x = 1$, using 36% deuterated

$(R)\text{-}\beta$-methylphenethylamine, d_4-methanol, and 48% DBr solution in D_2O instead of $(R/S)\text{-}\beta$-methylphenethylamine, methanol, and HBr aqueous solution, respectively. In addition, an achiral molecule-incorporated 2D-OIHP copper bromide named $(\text{PPA})_2\text{CuBr}_4$ (PPA-Br), where PPA^+ represents a 3-phenylpropylammonium ion, was synthesized for comparison with the chiral molecule-incorporated 2D-OIHP bromide. The single crystals of PPA-Br were synthesized by a procedure similar to that for the sample of $x = 1$ but with 3-phenylpropylamine instead of $(R/S)\text{-}\beta$-methylphenethylamine. The crystal structures were confirmed by single-crystal x-ray diffraction analysis of $(R/S\text{-MPA})_2\text{Cu}(\text{Cl}_{1-x}\text{Br}_x)_4$ (Tables S1–S7 in the Supplemental Material [43]), $D\text{-}R\text{-MPA-Br}$ (Tables S8 and S9 in the Supplemental Material), and PPA-Br (Table S10 in the Supplemental Material). Refinement of cell parameters and data reduction were performed with the CrysAlisPro software package [44]. The crystal structures of $(R/S\text{-MPA})_2\text{CuBr}_4$ at low temperatures were measured at BL-8B of the Photon Factory, High Energy Accelerator Research Organization (KEK), and at BL02B1 of SPring-8. Refinement of cell parameters and data reduction were performed with the RAPID software package. Crystal structures were solved by direct methods (SHELXT) [45] and refined using the OLEX crystallographic software package with full-matrix least-squares F^2 values [46].

The powder x-ray diffraction (PXRD) pattern was collected using a RIGAKU Ultima IV diffractometer with Cu $K\alpha$ radiation ($\lambda = 1.5418\,\text{Å}$) at room temperature. It was confirmed that the samples used in this study were in single phase by checking that the observed PXRD patterns coincide with the calculated patterns from the crystal structures obtained from the single-crystal structural analyses (Fig. S1 in the Supplemental Material [43]).

B. Magnetic measurements

Magnetization and alternating current (AC) magnetic susceptibility measurements were conducted on the single crystals using a quantum-design superconducting quantum interference device magnetometer (MPMS-XL). Magnetization and AC magnetic susceptibility were measured between 2 and 20 K under magnetic fields parallel and perpendicular to the ab plane, which in turn was parallel and perpendicular to the $[\text{CuX}_4]^{2-}$ layer ($X = \text{Cl}$, Br) of the 2D-OIHP copper halides. Direct current (DC) magnetic susceptibility measurements were performed with the polycrystal samples in 1000 Oe between 2 and 300 K.

C. Neutron diffraction measurements

Neutron diffraction measurements were conducted for the single crystals of $D\text{-}R\text{-MPA-Br}$ ($\sim7\,\text{mm} \times \sim4\,\text{mm} \times \sim300\,\mu\text{m}$) at 0 Oe in the temperature range of 4.3–16 K using the time-of-flight neutron diffractometer SENJU, installed at the Materials and Life Science Experimental Facility (MLF), Japan Proton Accelerator Research Complex (J-PARC), Japan. To investigate multiple magnetic phases appearing below 10 K in the magnetic field range of 0–800 Oe, magnetic modulation vectors (Q) were sought by measuring

the small-angle neutron scattering (SANS) profiles for the single crystals of D-R-MPA-Br around $Q = 0$ on TAIKAN at J-PARC [47].

III. RESULTS AND DISCUSSION

A. Structural analysis of $(R/S\text{-MPA})_2\text{Cu}(\text{Cl}_{1-x}\text{Br}_x)_4$

Figures 1(a) and 1(b) show the low-temperature crystal structures of $(R/S\text{-MPA})_2\text{CuBr}_4$ at 30 K. Theses crystal structures are almost unchanged from that at 103 K. (Figs. S2, S3 and Tables S11, S12, and S13 in the Supplemental Material). Similar to the previously reported structures of $(R/S\text{-MPA})_2\text{CuCl}_4$ [37], they have been confirmed to possess 2D-OIHP structures and belong to the triclinic space group $P1$, exhibiting both chirality and polarity (Tables S1 and S2 in the Supplemental Material). One of the characteristics is that the nearly square lattice appears in the $\text{Cu}X_2$ plane as found in the cell parameters of a, b and γ of $(R/S\text{-MPA})_2\text{Cu}X_4$ (X = Cl, Br) (Figs. S2(a), S2(c) and Tables S1, S2) although the overall symmetry of the crystal structures is low: a triclinic structure. It is also noteworthy that the bond angles of $\angle$Cu-Br-Cu in CuBr_2 plane of $(R/S\text{-MPA})_2\text{CuBr}_4$ are almost identical to those of $\angle$Cu-Cl-Cu in CuCl_2 plane of $(R/S\text{-MPA})_2\text{CuCl}_4$ [Fig. S3(a) and Tables S11, S12, and S13 in the Supplemental Material]. On the other hand, the bond length of Cu–X (X = Cl, Br) and the atomic distance between the neighboring Cu ions are longer in X = Br compared with those in X = Cl, reflecting difference of ionic radius between Br^- and Cl^-.

The atomic arrangements in the unit cells formed an inversion relationship between $(R\text{-MPA})_2\text{CuBr}_4$ and $(S\text{-MPA})_2\text{CuBr}_4$ [Figs. 1(a) and 1(b)]. $(R/S\text{-MPA})_2\text{CuBr}_4$ has an alternative stacking mode consisting of inorganic $[\text{CuBr}_4]^{2-}$ layers with corner-sharing CuBr_6 octahedra and double layers of $R/S\text{-MPA}^+$ along the c axis [Figs. 1(a) and 1(b)]. The $R/S\text{-MPA}^+$ ions are connected with the $[\text{CuBr}_4]^{2-}$ layers through N−H⋯Br hydrogen bonds. Reflecting the Jahn-Teller effect of the $3d$-hole orbitals of the Cu^{2+} ions, the local coordination of CuBr_6 in $(R/S\text{-MPA})_2\text{CuBr}_4$ consists of two short and two long in-plane Cu–Br bonds and two short out-of-plane Cu–Br bonds [Figs. 1(c), 1(d), and S4 in the Supplemental Material]. In the $[\text{CuBr}_4]^{2-}$ layer, the elongated diagonal Br–Cu–Br bonds and compressed diagonal Br–Cu–Br bonds in the CuBr_6 octahedra are arranged alternatively almost along the [110] or [1–10] directions [Figs. 1(c), 1(d), and S4 in the Supplemental Material]. The bond angle of $\angle$Cu-Br-Cu along the [110] is $\sim 180°$ (Table S11 in the Supplemental Material), indicating that CuB_6-octahedra do not rotate within the $[\text{CuBr}_4]^{2-}$ layer around the c^* axis. On the other hand, the bond angle of $\angle$Cu-Br-Cu along [1–10] is $\sim 169°$ (Table S11 in the Supplemental Material), producing polar deformation along the [110] as similar with $(R/S\text{-MPA})_2\text{CuCl}_4$ (Figs. S4 and S5 in the Supplemental Material) [37].

Figures 2(a)–2(e) show the crystal structures of the solid solutions produced by halogen atom substitution, specifically $(R\text{-MPA})_2\text{Cu}(\text{Cl}_{1-x}\text{Br}_x)_4$ (x = 0, 0.25, 0.5, 0.75, and 1), at 293 K. Every composition of the compound has been checked to maintain the 2D-OIHP structure and triclinic space group $P1$ (Tables S1–S7 in the Supplemental Material). In addition, the crystal structure of $x = 1$ has been confirmed to be consistent with that reported at 300 K [48]. In the Br-
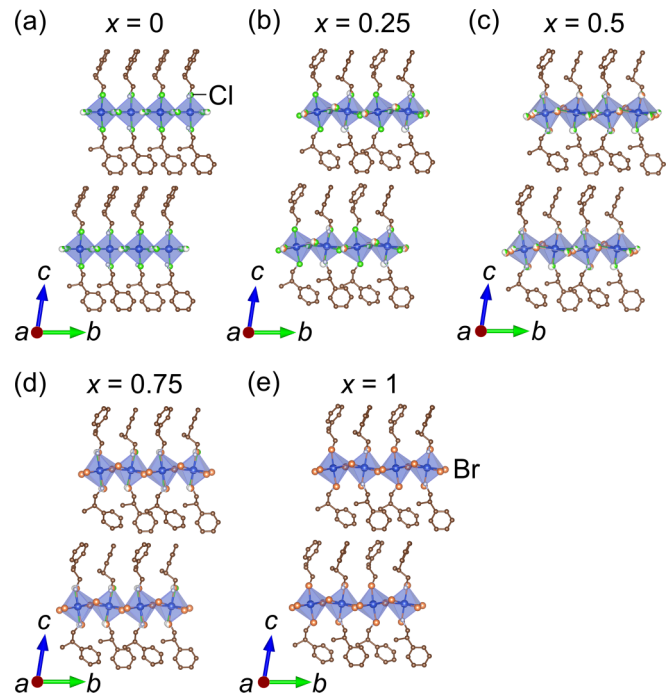

FIG. 2. Crystal structures at 293 K, projected along the a axis of $(R\text{-MPA})_2\text{Cu}(\text{Cl}_{1-x}\text{Br}_x)_4$ for (a) $x = 0$, (b) $x = 0.25$, (c) $x = 0.5$, (d) $x = 0.75$, and (e) $x = 1$. Yellowish green atoms represent Cl.

substituted compounds (x = 0.25, 0.5, 0.75, and 1), there is a buckling of $\text{Cu}(\text{Cl}_{1-x}\text{Br}_x)_6$-octahedra within the inorganic $[\text{Cu}(\text{Cl}_{1-x}\text{Br}_x)_4]^{2-}$ layers around 293 K, which is induced mainly by rotation of $\text{Cu}(\text{Cl}_{1-x}\text{Br}_x)_6$-octahedra around the [1–10] axis [Figs. 2 and S6(c) in the Supplemental Material]. In particular, the detail structural parameters of $(R\text{-MPA})_2\text{CuBr}_4$ ($x = 1$) at 293 K are summarized in Tables S14 and S15 in the Supplemental Material. Among them, the buckling of CuBr_6-octahedra around the [1–10] axis appears as deviation from $180°$ in the bond angles of $\angle$Cu-Br-Cu along [110] in $(R\text{-MPA})_2\text{CuBr}_4$ ($x = 1$) (Table S14 in the Supplemental Material). However, this buckling is found to be suppressed by lowering temperature for $x = 1$, as shown in Figs. 1(a) and S6(d) in the Supplemental Material: The bond angles of $\angle$Cu-Br-Cu along [110] changes to $\sim 180°$ below 103 K [Fig. S3(a) and Tables S11 and S12 in the Supplemental Material].

B. Magnetic characteristics of $(R\text{-MPA})_2\text{CuCl}_4$ ($x = 0$)

As reported in the previous studies [36,37], $x = 0$ exhibits ferromagnetic characteristics. When a magnetic field ($\boldsymbol{H}$) of 1000 Oe is applied parallel and perpendicular to the ab plane, the magnetization ($\boldsymbol{M}$) rapidly increases below ~ 7 K, as shown in Figs. 3(a) and S7 in the Supplemental Material. The $\boldsymbol{H}$ dependence of $\boldsymbol{M}$ is quite soft magnetic, and hysteresis curve in the $\boldsymbol{H}$ parallel to the ab plane could not be observed despite the measurements at a fine field step of 5 Oe (Fig. S8 in the Supplemental Material). The DC magnetic susceptibility (χ) measured for polycrystalline sample follows the Curie-Weiss law with a positive Weiss temperature (θ_w), indicating ferromagnetic exchange interaction (Fig. S9 in the
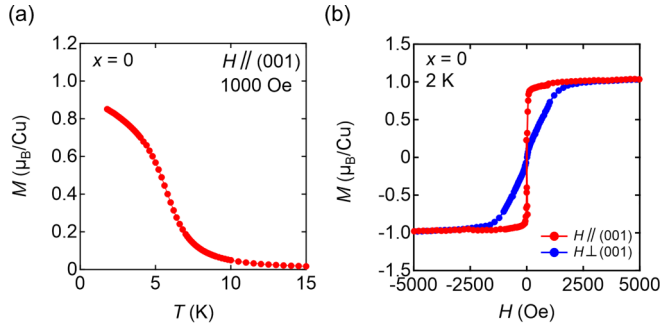
FIG. 3. Magnetization of $(R\text{-MPA})_2\text{CuCl}_4$ ($x = 0$). (a) Temperature dependence of magnetization in a magnetic field of 1000 Oe, parallel to the ab plane. (b) Magnetic field dependence of magnetization at 2 K. Red- and blue-closed circles represent the magnetizations in the $\boldsymbol{H}$-parallel and the $\boldsymbol{H}$-perpendicular configurations, respectively.

Supplemental Material). The θ_w estimated by the fitting for the $1/\chi$ above 150 K is 24.4 K, and the effective moment is 1.66 μ_B, which is close to the value 1.5 μ_B expected from Cu^{2+} ($S = 1/2$).

Figure 3(b) shows the $\boldsymbol{H}$ dependence of $\boldsymbol{M}$ for $x = 0$ at 2 K, with $\boldsymbol{H}$ applied parallel and perpendicular to the ab plane (defined as $\boldsymbol{H}$-parallel and $\boldsymbol{H}$-perpendicular configurations hereafter). In the $\boldsymbol{H}$-parallel configuration, the $\boldsymbol{M}$ immediately saturates to the value for the full magnetic moment of Cu^{2+} with $S = 1/2$ (1 μ_B/Cu) at approximately 1000 Oe. Magnetic anisotropy within the ab plane were confirmed to be negligible by comparing the $\boldsymbol{H}$ dependence of $\boldsymbol{M}$ in [110] and that in [1–10] (Fig. S10 in the Supplemental Material). In contrast, the $\boldsymbol{M}$ saturates to 1 μ_B/Cu at approximately 2400 Oe in the $\boldsymbol{H}$-perpendicular configuration. These facts indicate an easy plane magnetic anisotropy in $x = 0$.

The magnetic anisotropy also appears in the AC magnetic susceptibilities. Figures 4(a) and 4(b) show the temperature dependence of the real part of AC magnetic susceptibilities (χ') for the $\boldsymbol{H}$-parallel and $\boldsymbol{H}$-perpendicular configurations, respectively. In the $\boldsymbol{H}$-parallel configuration, a single peak anomaly was observed at each $\boldsymbol{H}$ in the range of 4–7 K, below 1000 Oe. Because the peak position coincides with the temperature at which $\boldsymbol{M}$ begins to increase [Figs. 3(a) and 4(a)], the positions of the peak anomalies in χ' should correspond to the temperature at which a magnetic phase transition from the paramagnetic to the ferromagnetic (FM) phase occurs. In contrast, the peak anomaly separates into two cusps above 200 Oe in the $\boldsymbol{H}$-perpendicular configuration. In the $\boldsymbol{H}$ dependence of χ', broad shoulder anomalies were observed at approximately ± 400 and ± 1000 Oe at 4 and 2 K, respectively, in addition to a sharp peak at 0 Oe due to the FM order [Fig. 4(c)].

Figures 5(a) and 5(b) show the magnetic phase diagrams for $x = 0$ at the peak/cusp positions of χ'. As shown in Fig. 5(a), the FM phase appears below 4–7 K, and the region of the FM phase expands with the increasing strength of $\boldsymbol{H}$ parallel to the ab plane. In contrast, another phase, named the spin-flopped ferromagnetic (SF) phase, appears above 200 Oe in the $\boldsymbol{H}$-perpendicular configuration, as shown in Fig. 5(b). Considering that $x = 0$ has an easy plane magnetic anisotropy and the $\boldsymbol{M}$ immediately saturates to the value of the full moment of Cu^{2+} (1 μ_B/Cu) in the $\boldsymbol{H}$-parallel configuration as shown in Fig. 3(b), FM spins should exist mainly in the ab plane in the FM phase. On the other hand, although the higher $\boldsymbol{H}$ is necessary for $\boldsymbol{M}$ saturation than that in the $\boldsymbol{H}$-parallel configuration, the $\boldsymbol{M}$ rapidly saturates to 1 μ_B/Cu also in the $\boldsymbol{H}$-perpendicular configuration. Thus, the SF phase, which appears in the $\boldsymbol{H}$-perpendicular configuration, could be a magnetic-field-induced FM phase, in which FM spins are speculated to be flopped from the ab plane. In fact, a metamagneticlike change of slope is found around 1000 Oe, where
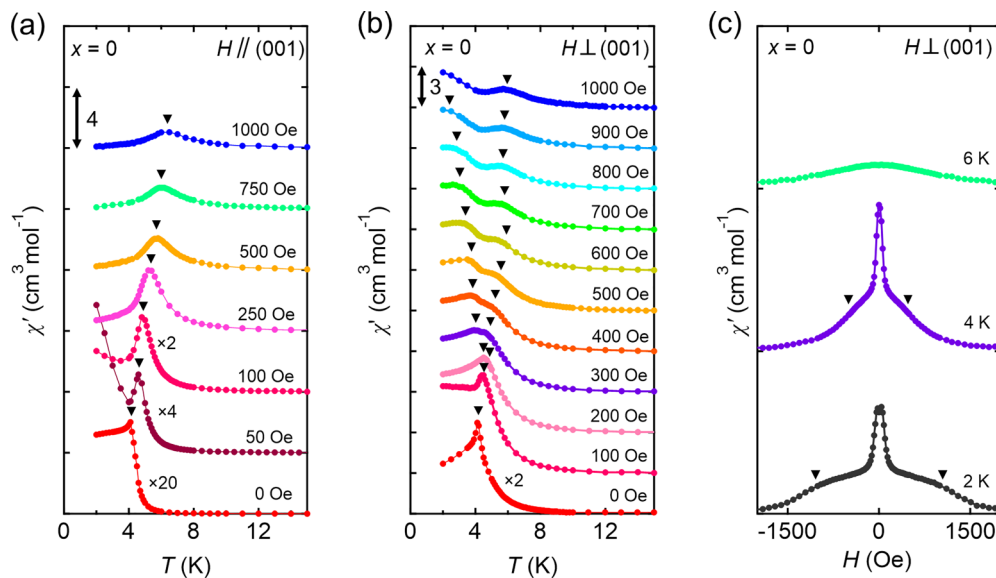

FIG. 4. Real part of AC magnetic susceptibility (χ') of $(R\text{-MPA})_2\text{CuCl}_4$ ($x = 0$). Temperature dependence of χ' measured in the (a) $\boldsymbol{H}$-parallel and (b) $\boldsymbol{H}$-perpendicular configurations. (c) Magnetic field dependence of χ' measured in the $\boldsymbol{H}$-perpendicular configuration. The closed black triangles in (a)–(c) show the peak/cusp positions used for producing the magnetic phase diagrams.

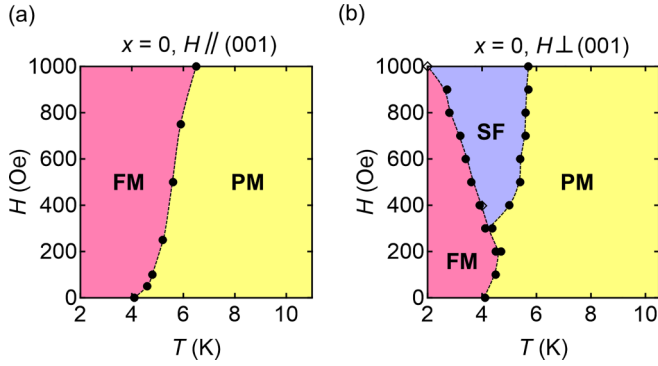FIG. 5. Magnetic phase diagrams of $(R\text{-MPA})_2\text{CuCl}_4$ ($x = 0$) in the (a) $\boldsymbol{H}$-parallel and (b) $\boldsymbol{H}$-perpendicular configurations. FM, PM, and SF in the phase diagram represent the ferromagnetic phase, paramagnetic phase, and spin-flopped ferromagnetic phase, respectively. The closed circles and open diamonds represent the peak/cusp anomaly positions observed in the temperature and magnetic field dependence plots of χ', respectively.

χ' has a bump structure, in magnetization at 2 K (Fig. S11 in the Supplemental Material). However, since the observed variation is so small, it is speculated that the crossover like gradual spin direction change between two-types of spin canted phase would occur in the spin-flop transition of $x = 0$.

C. Magnetic characteristics of $(R\text{-MPA})_2\text{CuBr}_4$ ($x = 1$)

Considering the alternating alignment of the elongated/compressed Br–Cu–Br bonds within the $[\text{CuBr}_4]^{2-}$ layer [Figs. 1(c) and 1(d)], the FMI, which is induced by the orbital ordering of orthogonal Cu $3d$-hole orbitals, should appear also in $x = 1$. Figures 6(a) and 6(b) show the temperature dependence of $\boldsymbol{M}$ for $x = 1$ in the $\boldsymbol{H}$-parallel and $\boldsymbol{H}$-perpendicular configurations, respectively. As expected from FMI, a rapid growth of $\boldsymbol{M}$ is observed below ~ 10 K in both the $\boldsymbol{H}$-parallel and the $\boldsymbol{H}$-perpendicular configurations (Fig. 6). In addition, a positive Weiss temperature, $\theta_w = 34.4$ K, is also observed in χ measured for polycrystalline sample as in $x = 0$ (Fig. S12 in the Supplemental Material). The effective moment estimated from Curie-Weiss fitting above 150 K is $1.68\,\mu_B$, which is close to the value $1.5\,\mu_B$ expected from Cu^{2+} ($S = 1/2$). Similar to $x = 0$, easy
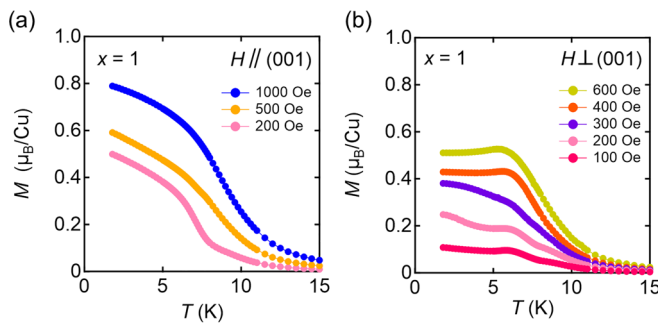

FIG. 6. Temperature dependence of magnetization for $(R\text{-MPA})_2\text{CuBr}_4$ ($x = 1$). Magnetization measured in the (a) $\boldsymbol{H}$-parallel and the (b) $\boldsymbol{H}$-perpendicular configurations.

plane magnetic anisotropy is also found in the temperature and magnetic field dependence of $\boldsymbol{M}$ (Figs. 6 and S13 in the Supplemental Material). In the $\boldsymbol{H}$-perpendicular configuration, the cusp/bending shape anomalies appear in the temperature dependence of $\boldsymbol{M}$ for $x = 1$ at ~ 6 K [Fig. 6(b)]. The $\boldsymbol{H}$ dependence of $\boldsymbol{M}$ is quite soft magnetic, and hysteresis curve in the $\boldsymbol{H}$-parallel configuration to the ab plane could not be observed also in $x = 1$ (Fig. S14 in the Supplemental Material).

To investigate the characteristics of the magnetic anomalies in the low $\boldsymbol{H}$ range, χ' was measured for $x = 1$ in the $\boldsymbol{H}$-perpendicular configuration. Figures 7(a) and 7(b) show the temperature dependence of χ' with an $\boldsymbol{H}$ below 1000 Oe. In contrast to $x = 0$, the behavior of χ' for $x = 1$ below 300 Oe is far more complicated [Figs. 7(a) and 7(b)]. In detail, two peak anomalies are observed at ~ 6 and 9 K at 0 Oe, whereas an additional peak appears at a lower temperature in the $\boldsymbol{H}$ range from 100 Oe to 225 Oe [Fig. 7(a)]. Upon increasing $\boldsymbol{H}$, the number of peak anomalies decrease to two at 300 Oe and one above 400 Oe [Fig. 7(b)]. We have also measured the $\boldsymbol{H}$ dependence of χ', where two types of peak anomalies are observed at 0 Oe and in the $|\boldsymbol{H}|$ range of 240–340 Oe, below 8 K [Fig. 7(c)].

Comparing the χ' of $x = 1$ with that of $x = 0$ under an out-of-plane $\boldsymbol{H}$, the number of peak anomalies increases in the low $\boldsymbol{H}$ regime for $x = 1$. This phenomenon indicates that multiple magnetic phases exist at $x = 1$ along with several successive magnetic phase transitions, whereas only a ferromagnetic phase transition occurs at $x = 0$ with an $\boldsymbol{H}$ below ~ 200 Oe. In perovskite analogs of transition metal compounds, it is known that the changes of structural parameters, such as bond angle and bond length etc., could affect the magnetic exchange interactions, producing multiple magnetic phases as observed in $(R\text{-MPA})_2\text{CuBr}_4$. In this study, we considered the four possible mechanisms and attributed the appearance of multiple magnetic phases to the competition between the FMI and DMI.

As the first possible mechanism, insulator-metal transition could be mentioned as a simple possible origin of magnetic phase change [49], since bond angles of $\angle M\text{-}X\text{-}M$ (M : transition metal, X : ligand atom) and bond length of $M\text{-}X$ modulate bandwidth of the compounds. However, in the case of $(R\text{-MPA})_2\text{Cu}X_4$ ($X = \text{Cl, Br}$), because the bond angles of $\angle M\text{-Cu-}M$ is almost same between the chloride ($x = 0$) and the bromide ($x = 1$) as shown in Tables S16 and S17, and both compounds are insulator, the scenario based on the insulator-metal transition is not applicable.

The second possible scenario includes competing interactions between superexchange interaction and double exchange interaction that is well-known in the hole-doped perovskites of manganese oxides [50]. In this case, the phase stability of the antiferromagnetic (AFM) insulating state with charge-orbital order and FM metallic state compete with each other and afford complex multiple phases depending on the bond angles of $\angle\text{Mn-O-Mn}$ and hole concentration. However, taking into account that the double exchange interaction is an interaction that appears in a mixed valence state with localized spins in t_{2g} orbitals, such as Mn^{3+} and Mn^{4+}, this mechanism also cannot be applied to $(R\text{-MPA})_2\text{Cu}X_4$ ($X = \text{Cl, Br}$) because $R\text{-MPA}^+$ is monovalent organic cation, and the valence of copper ions
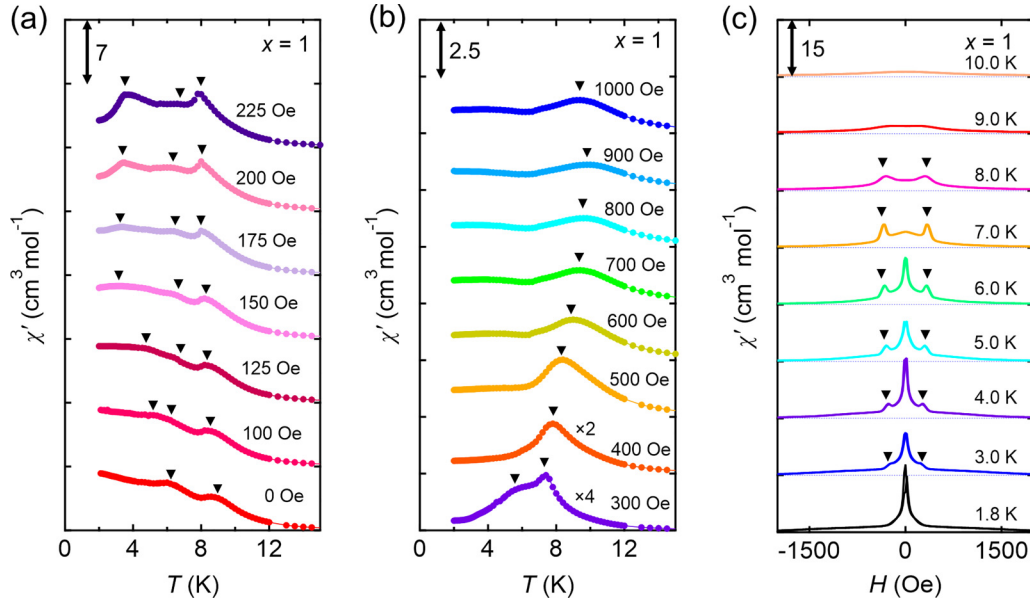
FIG. 7. Real part of AC magnetic susceptibility (χ') of (R-MPA)$_2$CuBr$_4$ ($x = 1$) in the $\boldsymbol{H}$-perpendicular configuration. Temperature dependence of χ' for magnetic fields in the range of (a) 0–225 Oe and (b) 300–1000 Oe. (c) Magnetic field dependence of χ' at 1.8–10.0 K. The closed black triangles in (a)–(c) show the peak/cusp positions used for producing the magnetic phase diagram.

is divalent (Cu^{2+}) with only one-hole in e-orbital for both chloride and bromide.

As the third mechanism producing multiple magnetic phases in insulating transition metal compounds with uniform valent transition metal ion, we can mention the competition between the nearest neighbor FM and the next nearest neighbor AFM interactions that is found in perovskite RMnO$_3$ (R: rare earth) [51]. In this mechanism, the variation of ∠Mn-O-Mn in MnO$_2$ plane induced by the in-plane rotation of MnO$_6$-octahedra changes the orbital overlap of the orthogonal orbital ordering state with FM interaction between nearest neighboring Mn sites. The modulation of orbital overlap produces additional AFM interaction between the next nearest neighboring Mn sites, generating competition between FM and AFM interactions. In such frustrated situation, long period magnetic structures, such as sinusoidal and spiral spin structures, are possible and experimentally observed in RMnO$_3$. In the case of (R-MPA)$_2$CuX_4 ($X =$ Cl, Br), this mechanism could become the origin forming multiple magnetic phases. However, as displayed in Figs. S4, S5, and Tables S11, S12, and S13, since no in-plane rotation of CuX_6 octahedra in the [CuBr$_4$]$^{2-}$ layer occurs in (R-MPA)$_2$CuX_4 ($X =$ Cl, Br), this mechanism can be also excluded as an origin of observed multiple phases.

Considering these facts, the difference of χ' behavior between $x = 0$ and $x = 1$ at low $\boldsymbol{H}$ could be attributed to the generation of multiple magnetic phases induced by competition between the FMI and DMI. Taking into account that the DMI originates from the combination of exchange interactions and SOC, the DMI is expected to be more pronounced with a stronger SOC for $x = 1$ with a larger-atomic-number halogen (Br) than that for $x = 0$ (Cl). Although the halogens, such as Br and Cl, are nonmagnetic ligand atoms, we can find the hybridization of Cu d-orbital and halogen p-orbital

in the valence band reported by first-principles calculation for 2D-OIHP Cu halides [52,53]. In fact, d-p hybridization effect for Cu and halogen atoms could be also found in the magnetic characteristics in experiments. For example, although the Cu-Cu distance of bromide ($x = 1$) is longer than that of chloride ($x = 0$) as shown in Tables S12 and S13, the bromide ($x = 1$) has the higher magnetic transition temperature and the Weiss temperature than those of the chloride ($x = 0$) as displayed in Figs. 4(a), 7(a), S9, and S12: the magnetic transition temperature are ∼4 K ($x = 0$) and ∼9 K ($x = 1$) and Weiss temperature are 24.4 K ($x = 0$) and 34.4 K ($x = 1$). Taking into account that the bond angles of ∠Cu-X-Cu are almost same for the chloride ($x = 0$) and the bromide ($x = 1$) as shown in Fig. S3(a) and, Tables S12, S13, the observed results could be attributed to the presence of orbital hybridization between Cu and ligand halogen atoms. Therefore, the electronic states of magnetic Cu ions should be also affected by the SOC change in halogen atoms through the d-p orbital hybridizarion between Cu and halogen atoms, leading to DMI enhancement.

The FMI aligns the spins in parallel to form a collinear spin structure, whereas the DMI attempts to tilt the spins to form a noncollinear/noncoplanar spin structure. Hence, the two interactions are expected to compete with each other to form complicated long-period magnetic structures such as helical spin structures [13,14] and magnetic skyrmions [15–18].

D. Magnetic phase change of (R-MPA)$_2$Cu(Cl$_{1-x}$Br$_x$)$_4$

The systematic tunability of the SOC strength was achieved by changing the substitution ratio of Cl to Br in (R-MPA)$_2$Cu(Cl$_{1-x}$Br$_x$)$_4$. Figures 8(a), 8(b), and 8(c) show the temperature dependence of χ' in the $\boldsymbol{H}$-perpendicular configuration for $x = 0.25$, $x = 0.5$, and $x = 0.75$, respectively. Similar to $x = 0$, a single peak anomaly appears below
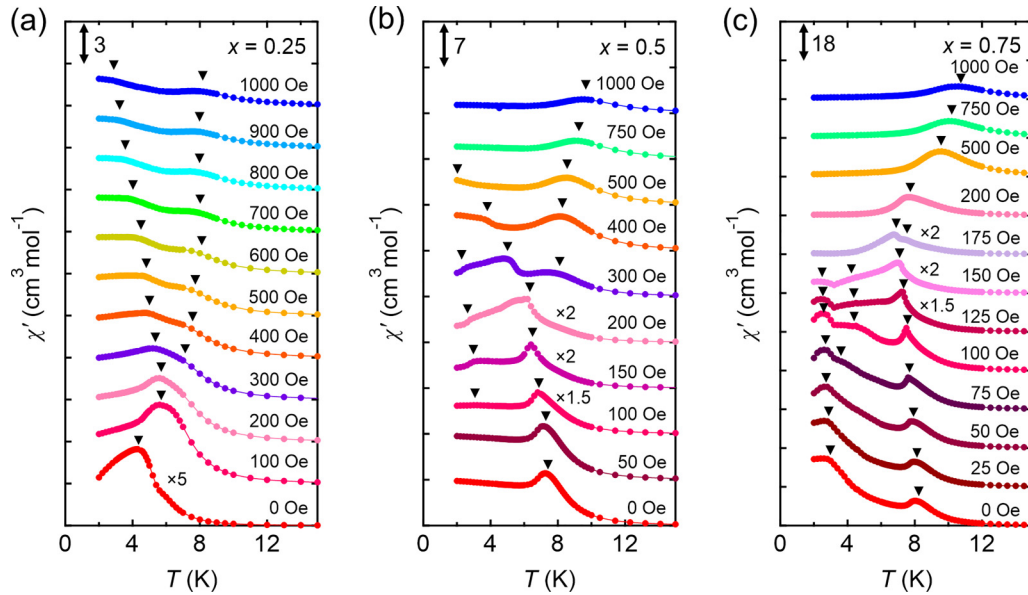
FIG. 8. Temperature dependence of the real part of AC magnetic susceptibility (χ') of $(R\text{-MPA})_2\text{Cu}(\text{Cl}_{1-x}\text{Br}_x)_4$ for (a) $x = 0.25$, (b) $x = 0.5$, and (c) $x = 0.75$ in the $\boldsymbol{H}$-perpendicular configuration. The closed black triangles in (a)–(c) show the peak/cusp positions used for producing the magnetic phase diagrams.

200 Oe and separates into two peaks above 300 Oe in $x = 0.25$ [Fig. 8(a)]. Upon further substitution of Cl with Br, an additional peak appears at approximately 3 K below 300 and 150 Oe in the χ' of $x = 0.5$ and $x = 0.75$, respectively [Figs. 8(b) and 8(c)]. Specifically, the characteristics of χ' of $x = 0.5$ seems to be a combination of those for $x = 0$ and $x = 1$. In $x = 0.5$, multiple peak anomalies, which are similar to $x = 1$, appear below 300 Oe. On the other hand, the peak around 7 K for $x = 0.5$ below 200 Oe seems to split into two peaks above 300 Oe as observed for the single peak at approximately 4 K for $x = 0$ [Fig. 8(b)]. However, the features of χ' in $x = 0.75$ are analogous to those of $x = 1$; the number of peak anomalies for $x = 0.75$ increases from two to three and reduces to one as the applied $\boldsymbol{H}$ increases [Fig. 8(c)].

The magnetic phase diagrams, which are produced based on the peak/cusp positions in χ' (Figs. 7, 8, and S15 in the Supplemental Material), are shown for $x = 0.25$, 0.5, 0.75, and 1 in Fig. 9. The three phases appearing at $x = 0.25$ [Fig. 9(a)] are assigned to the FM, SF, and paramagnetic (PM) phases because the magnetic behavior is qualitatively similar to that of $x = 0$ [Fig. 5(b)]. Considering that the systematic variation of magnetic phase diagrams associates with the degree of Br substitution [Figs. 5(b) and 9], the magnetic order phases in the high $\boldsymbol{H}$ region for compounds with $x \geqslant 0.5$ could be assigned as SF phases [Figs. 9(b)–9(d)]. However, new magnetic order phases other than the FM phase are observed in the low $\boldsymbol{H}$ region; for $x = 0.5$, $x = 0.75$, and $x = 1$, a new I-phase appears at lower temperatures in comparison to the FM phases [Figs. 9(b)–9(d)]. Furthermore, $x = 1$ exhibits another $\boldsymbol{H}$-induced phase, namely phase II, which is surrounded by the FM, SF, and I-phases [Fig. 9(d)]. This systematic variation in the magnetic phases should be ascribed to the pronounced competition between FMI and DMI induced by enhanced SOC associated with the increase of Br ratio.

Long-period magnetic structures, such as the helical spin structures and magnetic skyrmions, can be induced when FMI and DMI compete with each other [13–18]. Therefore, we performed neutron diffraction measurements for the magnetic order phases of $x = 1$ to investigate the magnetic modulation vector, which is a characteristic feature of long-period magnetic structures. For this purpose, a deuterated bromide (D-R-MPA-Br), which is isostructural with $x = 1$, was prepared. (Fig. S16 and Tables S8 and S9 in the Supplemental Material). In the experiment, magnetic superlattice reflections were investigated in the $hk0$ plane in the reciprocal lattice space as the crystal structure of $(R\text{-MPA})_2\text{CuBr}_4$ is anisotropic 2D-OIHP one, where the in-plane magnetic interactions should be dominant. However, the superlattice reflection could not be clearly recognized in any magnetic phases within the resolution limit of the diffractometer used in the experiments. However, an increase in the peak intensity was observed with a decrease in the temperature around the fundamental reflection at 0 Oe (Fig. S17 in the Supplemental Material).

Considering that the ground state of a noncentrosymmetric ferromagnetic system could be a helical spin structure [54], the I phase observed as the lowest temperature phase for $x > 0.25$ compounds is speculated as a helical spin phase induced by the competition between DMI and FMI, where the former is enhanced by the Br substitution. Taking into account that the magnetic wave number Q for the helical spin structure in the ground state is determined by the strength ratio of DMI to FMI, the observed neutron diffraction result might be ascribed to the formation of a super long-period helical spin structure with a nearly zero magnetic wave number ($Q \sim 0$) resulting from a much weaker DMI compared to FMI: the Q is associated with a parameter $|D/J|$, where J and D denote the interaction constants of FMI and DMI, respectively [55]. Similarly, the $\boldsymbol{H}$-induced II-phase at $x = 1$ could correspond
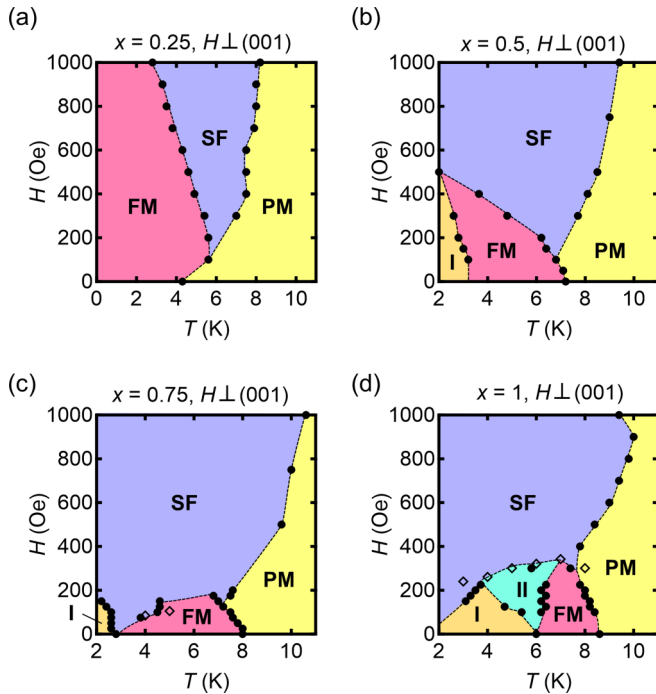
FIG. 9. Magnetic phase diagrams of $(R\text{-MPA})_2\text{Cu}(\text{Cl}_{1-x}\text{Br}_x)_4$ for (a) $x = 0.25$, (b) $x = 0.5$, (c) $x = 0.75$, and (d) $x = 1$ in the $\boldsymbol{H}$-perpendicular configuration. FM, PM, and SF in the phase diagram represent ferromagnetic phase, paramagnetic phase, and spin-flopped ferromagnetic phase, respectively. I and II in the magnetic phase diagram represent the additional magnetic phases in $x = 0.5$, 0.75, and 1. The positions of the closed circles and open diamonds were determined from the temperature and magnetic field dependence of χ', respectively.

to the formation of another super-long-period spin structure with a different Q. Identification of the magnetic modulation

vector of these new phases is a challenge that can be addressed in the future using measurement systems with higher resolution.

E. Magnetic characteristics of centrosymmetric $(\text{PPA})_2\text{CuBr}_4$ (PPA-Br)

The systematic variation of the magnetic order phases in $(R\text{-MPA})_2\text{Cu}(\text{Cl}_{1-x}\text{Br}_x)_4$ implies the existence of FMI-DMI competition and the importance of SOC in noncentrosymmetric systems. To support this assumption, we studied the magnetic characteristics of a centrosymmetric 2D-OIHP copper bromide, PPA-Br, in which achiral PPA^+ [Fig. 10(a)] was used as the incorporated molecular cation instead of chiral $R/S\text{-MPA}^+$ [Fig. 10(b)]. PPA-Br possesses a 2D-OIHP structure similar to $(R/S\text{-MPA})_2\text{CuBr}_4$ [Figs. 10(b) and S18 in the Supplemental Material] but crystalizes in a centrosymmetric triclinic space group $P-1$ (Table S10 in the Supplemental Material). In the crystal structure of PPA-Br, there is a buckling of CuBr_6-octahedra in the inorganic $[\text{CuBr}_4]^{2-}$ layers (Fig. S18 in the Supplemental Material). However, the bond angle of $\angle$Cu-Br-Cu along the [110] is $\sim180°$ as in the low temperature phase of $x = 1$ (Table S16 in the Supplemental Material), indicating that CuB_6-octahedra do not rotate within the $[\text{CuBr}_4]^{2-}$ layer around the c^* axis. On the other hand, although the $\angle$Cu-Br-Cu bond angle along [1–10] of PPA-Br also deviates from $180°$ similar to $x = 1$, it reflects the rotation of CuBr_6-octahedra around [110] axis rather than the polar deformation of CuBr_6 observed in $x = 1$. (Table S17 and Fig. S18 in the Supplemental Material).

Figures 10(c) and 10(d) show the temperature dependence of χ' and magnetic phase diagram of PPA-Br in the $\boldsymbol{H}$-perpendicular configuration, respectively. Ferromagnetic behavior was also observed (Fig. S19 in the Supplemental Material) with peak/cusp anomalies appearing in χ'
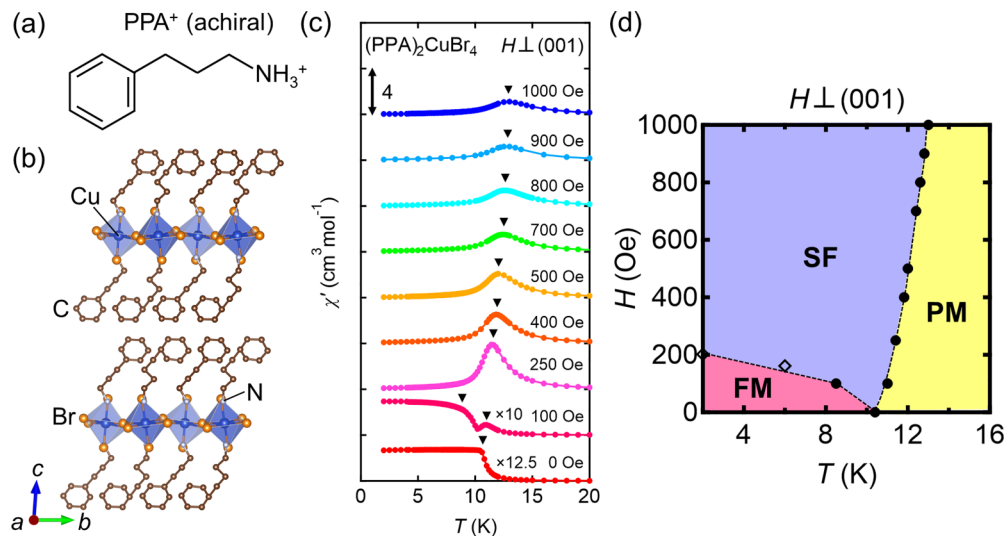

FIG. 10. Crystal structure and magnetic characteristics of centrosymmetric $(\text{PPA})_2\text{CuBr}_4$ (PPA-Br). (a) Molecular cation structure of achiral PPA^+. (b) Crystal structure projected along the a axis. (c) Temperature dependence of the real part of AC magnetic susceptibility (χ') in the $\boldsymbol{H}$-perpendicular configuration. The closed black triangles show the peak/cusp positions used for producing the magnetic phase diagram. (d) Magnetic phase diagram in the $\boldsymbol{H}$-perpendicular configuration. FM, PM, and SF in the phase diagram represent ferromagnetic, paramagnetic, and spin-flopped ferromagnetic phases, respectively. The positions of closed circles and open diamonds were determined from the temperature and magnetic field dependence of χ', respectively.

at the magnetic phase transition temperature [Fig. 10(c)]. In contrast to the noncentrosymmetric $x = 1$, complicated successive magnetic phase transitions are not observed in the low-H regime. In the case of PPA-Br, the buckling $CuBr_6$-octahedra in $[CuBr_4]^{2-}$ layer might affect magnetic interaction. However, due to absence of the in-plane rotation of $CuBr_6$-octahedra around the perpendicular axis to $[CuBr_4]^{2-}$ layer [Figs. S18(a), S(b) and Table S16 in the Supplemental Material], competition between FM and AFM exchange interactions as in RMnO$_3$ [51] should not occur, and the buckling of $CuBr_6$-octahedara would simply change the strength of the FM exchange interaction. In fact, we have confirmed that Curie-Weiss temperature for PPA-Br, $\theta_w = 33.5\,\text{K}$ (Fig. S20 in the Supplemental Material), is similar to that of $x = 1$, $\theta_w = 34.4\,\text{K}$, indicating that the effects of crystal structural difference caused by the buckling of $CuBr_6$-octahedra is negligible. These facts indicate the absence of FMI-DMI competition, despite the presence of strong SOC. These results support our hypothesis that the additional magnetic phases found at $x = 0.5$, 0.75, and 1 might be related to the long-period magnetic structures that occur as a result of the FMI-DMI competitions, which are only allowed in a noncentrosymmetric environment.

IV. SUMMARY

In summary, the strength tunability of the SOC by material design has been demonstrated in a series of chiral molecule-incorporated 2D-OIHP copper halides

$(R$-MPA$)_2$Cu$(Cl_{1-x}Br_x)_4$, with FMI. With increasing Br ratio, the magnetic phase diagrams are systematically transformed from an FMI dominant one to a complicated one with multiple phases arising owing to the competition between DMI and FMI. This hypothesis is supported by the observation of an FMI-dominated magnetic phase diagram in an achiral molecule-incorporated 2D-OIHP copper bromide with an inversion symmetry. As demonstrated in this study, controlling the noncentrosymmetry and SOC simultaneously using organic-inorganic hybrid systems could be a promising and rational way to develop topological materials with nontrivial spin structures such as magnetic skyrmions.

[1] D. Grundler, Phys. Rev. Lett. **84**, 6074 (2000).

[2] K. Ishizaka, M. S. Bahramy, H. Murakawa, M. Sakano, T. Shimojima, T. Sonobe, K. Koizumi, S. Shin, H. Miyahara, A. Kimura, K. Miyamoto, T. Okuda, H. Namatame, M. Taniguchi, R. Arita, N. Nagaosa, K. Kobayashi, Y. Murakami, R. Kumai, Y. Kaneko, Y. Onose, and Y. Tokura, Nat. Mater. **10**, 521 (2011).

[3] Y. Tokura and N. Nagaosa, Nat. Commun. **9**, 3740 (2018).

[4] G. L. J. A. Rikken and P. Wyder, Phys. Rev. Lett. **94**, 016601 (2005).

[5] T. Ideue, K. Hamamoto, S. Koshikawa, M. Ezawa, S. Shimizu, Y. Kaneko, Y. Tokura, N. Nagaosa, and Y. Iwasa, Nat. Phys. **13**, 578 (2017).

[6] F. Ando, Y. Miyasaka, T. Li, J. Ishizuka, T. Arakawa, Y. Shiota, T. Moriyama, Y. Yanase, and T. Ono, Nature (London) **584**, 373 (2020).

[7] Y. Li, Y. Li, P. Li, B. Fang, X. Yang, Y. Wen, D. X. Zheng, C. H. Zhang, X. He, A. Manchon, Z. H. Cheng, and X. X. Zhang, Nat. Commun. **12**, 540 (2021).

[8] T. Kimura, T. Goto, H. Shintani, K. Ishizaka, T. Arima, and Y. Tokura, Nature (London) **426**, 55 (2003).

[9] H. Katsura, N. Nagaosa, and A. V. Balatsky, Phys. Rev. Lett. **95**, 057205 (2005).

[10] I. A. Sergienko and E. Dagotto, Phys. Rev. B **73**, 094434 (2006).

[11] K. Taniguchi, N. Abe, T. Takenobu, Y. Iwasa, and T. Arima, Phys. Rev. Lett. **97**, 097203 (2006).

[12] T. Arima, J. Phys. Soc. Jpn. **76**, 073702 (2007).

[13] T. Moriya and T. Miyadai, Solid State Commun. **42**, 209 (1982).

[14] Y. Togawa, T. Koyama, K. Takayanagi, S. Mori, Y. Kousaka, J. Akimitsu, S. Nishihara, K. Inoue, A. S. Ovchinnikov, and J. Kishine, Phys. Rev. Lett. **108**, 107202 (2012).

[15] S. Mühlbauer, B. Binz, F. Jonietz, C. Pfleiderer, A. S. Rosch, A. Neubauer, R. Georgii, and P. Böni, Science **323**, 915 (2009).

[16] S. Seki, X. Z. Yu, S. Ishiwata, and Y. Tokura, Science **336**, 198 (2012).

[17] I. Kézsmárki, S. Bordács, P. Milde, E. Neuber, L. M. Eng, J. S. White, H. M. Rønnow, C. D. Dewhurst, M. Mochizuki, K. Yanai, H. Nakamura, D. Ehlers, V. Tsurkan, and A. Loidl, Nat. Mater. **14**, 1116 (2015).

[18] Y. Tokunaga, X. Z. Yu, J. S. White, H. M. Rønnow, D. Morikawa, Y. Taguchi, and Y. Tokura, Nat. Commun. **6**, 7638 (2015).

[19] A. Neubauer, C. Pfleiderer, B. Binz, A. Rosch, R. Ritz, P. G. Niklowitz, and P. Böni, Phys. Rev. Lett. **102**, 186602 (2009).

[20] N. Kanazawa, Y. Onose, T. Arima, D. Okuyama, K. Ohoyama, S. Wakimoto, K. Kakurai, S. Ishiwata, and Y. Tokura, Phys. Rev. Lett. **106**, 156603 (2011).

[21] T. Yokouchi, N. Kanazawa, A. Kikkawa, D. Morikawa, K. Shibata, T. Arima, Y. Taguchi, F. Kagawa, and Y. Tokura, Nat. Commun. **8**, 866 (2017).

[22] R. Aoki, Y. Kousaka, and Y. Togawa, Phys. Rev. Lett. **122**, 057206 (2019).

[23] J. Ahn, E. Lee, J. Tan, W. Yang, B. Kim, and J. Moon, Mater. Horiz **4**, 851 (2017).

[24] G. Long, C. Jiang, R. Sabatini, Z. Yang, M. Wei, L. N. Quan, Q. Liang, A. Rasmita, M. Askerka, G. Walters, X. Gong, J. Xing, X. Wen, R. Quintero-Bermudez, H. Yuan, G. Xing, X. R. Wang, D. Song, O. Voznyy, M. Zhang, S. Hoogland, W. Gao, Q. Xiong, and E. H. Sargent, Nat. Photon. **12**, 528 (2018).

[25] J. Ahn, S. Ma, J. Y. Kim, J. Kyhm, W. Yang, J. A. Lim, N. A. Kotov, and J. Moon, J. Am. Chem. Soc. **142**, 4206 (2020).

[26] J. Ma, C. Fang, C. Chen, L. Jin, J. Wang, S. Wang, J. Tang, and D. Li, ACS Nano **13**, 3659 (2019).

[27] J. Wang, C. Fang, J. Ma, S. Wang, L. Jin, W. Li, and D. Li, ACS Nano **13**, 9473 (2019).

[28] C.-K. Yang, W.-N. Chen, Y.-T. Ding, J. Wang, Y. Rao, W. Q. Liao, Y.-Y. Tang, P.-F. Li, Z.-X. Wang, and R.-G. Xiong, Adv. Mater. **31**, 1808088 (2019).

[29] P. J. Huang, K. Taniguchi, and H. Miyasaka, J. Am. Chem. Soc. **141**, 14520 (2019).

[30] P.-J. Huang, K. Taniguchi, and H. Miyasaka, Chem. Mater. **34**, 4428 (2022).

[31] P.-J. Huang, K. Taniguchi, M. Shigefuji, T. Kobayashi, M. Matsubara, T. Sasagawa, H. Sato, and H. Miyasaka, Adv. Mater. **33**, 2008611 (2021).

[32] R. Pan, X. Tang, L. Kan, Y. Li, H. Yu, and K. Wang, Nanoscale **15**, 3300 (2023).

[33] H. Lu, J. Wang, C. Xiao, X. Pan, X. Chen, R. Brunecky, J. J. Berry, K. Zhu, M. C. Beard, and Z. V. Vardeny, Sci. Adv. **5**, eaay0571 (2019).

[34] H. Lu, C. Xiao, R. Song, T. Li, A. E. Maughan, A. Levin, R. Brunecky, J. J. Berry, D. B. Mitzi, V. Blum, and M. C. Beard, J. Am. Chem. Soc. **142**, 13030 (2020).

[35] Y. H. Kim, Y. Zhai, H. Lu, X. Pan, C. Xiao, E. A. Gaulding, S. P. Harvey, J. J. Berry, Z. V. Vardeny, J. M. Luther, and M. C. Beard, Science **371**, 1129 (2021).

[36] B. Sun, X.-F. Liu, X.-Y. Li, Y. Zhang, X. Shao, D. Yang, and H.-D. Zhang, Chem. Mater. **32**, 8914 (2020).

[37] K. Taniguchi, M. Nishio, N. Abe, P. J. Huang, S. Kimura, T. Arima, and H. Miyasaka, Angew. Chem. Int. Ed. **60**, 14350 (2021).

[38] C. Bellitto, P. Filaci, and S. Patrizio, Inorg. Chem. **26**, 191 (1987).

[39] S. H. Park, I. H. Oh, S. Park, Y. Park, J. H. Kim, and Y. D. Huh, Dalton Trans. **41**, 1237 (2012).

[40] Y. Nakayama, S. Nishihara, K. Inoue, T. Suzuki, and M. Kurmoo, Angew. Chem. Int. Ed. **56**, 9367 (2017).

[41] A. A. Nugroho, Z. Hu, C. Y. Kuo, M. W. Haverkort, T. W. Pi, D. Onggo, M. Valldor, and L. H. Tjeng, Phys. Rev. B **94**, 184404 (2016).

[42] Y. Ito and J. Akimitsu, J. Phys. Soc. Jpn. **40**, 1333 (1976).

[43] See Supplemental Material at http://link.aps.org/supplemental/10.1103/PhysRevMaterials.8.024409 for the experimental methods, PXRD patterns, crystallographic parameters, DC magnetization, AC magnetic susceptibility, the result of neutron diffraction measurement.

[44] *CrysAlisPro* 1.171.38.43, Rigaku Corporation, Tokyo, 2015.

[45] G. M. Sheldrick, Acta Cryst. A 64, 112 (2008).

[46] *Olex 2* 1.3, OlexSys Ltd., 2019.

[47] S. Takata, J. Suzuki, T. Shinohara, T. Oku, T. Tominaga, K. Ohishi, H. Iwase, T. Nakatani, Y. Inamura, T. Ito, K. Suzuya, K. Aizawa, M. Arai, T. Otomo, and M. Sugiyama, JPS Conf. Proc. **8**, 036020 (2015).

[48] M. Takahashi, N. Hoshino, K. Sambe, T. Takeda, and T. Akutagawa, Inorg. Chem. **59**, 11606 (2020).

[49] M. Imada, A. Fujimori, and Y. Tokura, Rev. Mod. Phys. **70**, 1039 (1998).

[50] Y. Tokura and Y. Tomioka, J. Magn. Magn. Mater. **200**, 1 (1999).

[51] T. Kimura, S. Ishihara, H. Shintani, T. Arima, K. T. Takahashi, K. Ishizaka, and Y. Tokura, Phys. Rev. B **68**, 060403(R) (2003).

[52] D. Cortecchia, H. A. Dewi, J. Yin, A. Bruno, S. Chen, T. Baikie, P. P. Boix, M. Grätzel, S. Mhaisalkar, C. Soci, and N. Mathews, Inorg. Chem. **55**, 1044 (2016).

[53] J. H. Lee, S. H. Kim, K.-Y. Doh, E. H. Kim, and D. Lee, J. Am. Chem. Soc. **142**, 14859 (2020).

[54] O. Nakanishi, A. Yanase, A. Hasegawa, and M. Kataoka, Solid State Commun. **35**, 995 (1980).

[55] M. Kataoka, J. Phys. Soc. Jpn. **56**, 3635 (1987).